Revision 1

A Refined Monoclinic Structure for a Variety of "Hydrohematite"

Kristina M. Peterson[1*], Peter J. Heaney[1], Jeffrey E. Post[2], Peter J. Eng[3]

[1]Department of Geosciences, Pennsylvania State University, University Park, PA 16802

[2]Department of Mineral Sciences, Smithsonian Institution, Washington, D.C. 20560-0119

[3]Consortium for Advanced Radiation Sources, The University of Chicago, Chicago, IL 60637

*To whom correspondence should be addressed: kmp286@gmail.com

ABSTRACT

In ferruginous soils, nano- to micro-scale hematite (α-Fe_2O_3) plays a central role in redox processes and contaminant cycling. Hematite is known to incorporate structural OH^- and water, and the requisite charge balance is achieved by iron vacancies. Prior researchers have suggested that the defective hematite structures form unique phases called "protohematite" and "hydrohematite". Infrared and Raman spectroscopic studies have assigned a lower-symmetry space group to "hydrohematite" (*R*3*c*) relative to that of stoichiometric hematite (*R*-3*c*). However, the existence and structure of these phases have been contentious, largely due to the lack of *in situ* X-ray diffraction data.

Here we present a new structure refinement for "hydrohematite" precipitated hydrothermally at 200 ^oC in a monoclinic space group (*I*2/*a*) using time-resolved synchrotron X-ray diffraction (TR-XRD) data collected during the *in situ* hydrothermal precipitation of akaganéite and its transformation to stoichiometric hematite. Distinct peak splitting was observed in the "hydrohematite" diffraction patterns, indicating a violation of the 3-fold rotational symmetry. A monoclinic unit cell with parameters of a = 7.3951(10) Å, b = 5.0117(5) Å, c = 5.4417(7) Å, β = 95.666(5)° provided a good fit and significant reduction in χ^2 and R_{wp} relative to S.G. *R*-3*c*. Rietveld analyses revealed that water concentrations in the first-formed crystals of "hydrohematite" were comparable to water contents of akaganéite and goethite. Thus, the hydrothermal transformation of akaganéite to "hydrohematite" is promoted not by dehydration but by reconstruction of the oxygen framework.

Keywords: Hydrohematite, Protohematite, Hematite, Akaganéite, X-ray Diffraction

INTRODUCTION

Hematite (α-Fe_2O_3) is one of the most abundant iron oxide minerals on the Earth's surface. It is central to terrestrial redox processes and biogeochemical cycling, and it also is likely a significant constituent of the Martian regolith (Cornell and Schwertmann 2001; Christensen 2004; Boyd and Ellwood 2010; Potter et al. 2011; Shanker et al. 2011). Moreover, its relative ubiquity, low toxicity and stability over a wide variety of environments make hematite an important industrial material, and it is used in a range of applications such as catalysts, pigments, and semiconductors (Yanina and Rosso 2008; Liu et al. 2010; Gialanella et al. 2011; Cheng et al. 2012). Hematite often forms through the thermal or hydrothermal transformation of iron oxyhydroxides, such as ferrihydrite, goethite, and akaganéite. When derived from oxyhydroxides, hematite may retain significant concentrations of molecular water and hydroxyl groups (OH^-) within its structure (Cornell and Schwertmann 2001). These impurities can distort the hematite crystal structure on the nano- to microscale, thereby changing the physical properties and chemical reactivity (Dang et al. 1998; Jang et al. 2007; Landers and Gilkes 2007; Pailhé et al. 2008; Chernyshova et al 2010).

Early history -- turgite and hydrohematite. Several mineralogists of the mid-nineteenth century observed that hematite-like minerals are capable of sequestering high concentrations of water. In an 1844 paper, Hermann described a hydrous iron oxide mineral with 5.85 wt% H_2O from the copper mines near Bosgolovsk, in the Ural Mountains on the river Turga. As this quantity of water was half that found in "stilpnosiderite" ($Fe_2O_3 \cdot H_2O$, or what today we would call goethite), Hermann argued for a new mineral species name, "turgite", with the formula $Fe_2O_3 \cdot \frac{1}{2}H_2O$. Three years later, Breithaupt (1847) independently proposed the name "hydrohematite" for hematite-

like specimens from Bavaria and Prussia having ~5 wt% H_2O. Hermann and Breithaupt observed that this new species is identical to anhydrous hematite in its physical characteristics, particularly in its brick-red streak, except that "turgite" and "hydrohematite" violently decrepitate when heated. Over the next 70 years, geologists employed both "turgite" (or, rarely, "turite") and "hydrohematite" as valid mineral names to describe hydrated sesquioxides of Fe from localities around the world (e.g., Brush and Rodman 1867; Dana and Brush 1868; Killebrew 1879; Spencer 1919).

Posnjak and Merwin (1919) systematically investigated hydrous Fe oxides by a combination of wet chemical analysis and thermal dehydration, and they were the first to suggest that turgite and hydrohematite do not represent distinct mineral endmembers. Instead, they propose that these varieties are part of a solid solution between hematite and goethite. Following their study, the mineralogy community questioned the legitimacy of these terms as distinct mineral names. For example, in the 7th edition of Dana's *System of Mineralogy*, Palache et al. (1944) cite X-ray diffraction data to support their contention that "turgite" is synonymous with hematite and should be discredited. Nickel and Nichols (1991) list "turgite" as a nonspecies name synonymous with hematite, and today neither "turgite" nor "hydrohematite" is approved by the International Mineralogical Association. Instead, these terms are used informally by collectors as varietal names, especially for iridescent specimens.

Recent history -- protohematite and hydrohematite. Over the half-century following Posnjak and Merwin's study, chemists, materials scientists, and even the occasional geologist continued to describe hydrous varieties of hematite as "turgite" or "hydrohematite" (Kurnakow and Rode 1928; Hüttig and Strotzer 1936; Steinwehr 1969).

A more serious revival of interest in the crystallographic distinctions among hydrous Fe oxides developed in the 1980s. Numerous scientists have inferred that water and OH^- substitutions must modify the hematite crystal structure, and they have offered suggestions for the kinds of distortions that result (Wolska 1981; Gualtieri and Venturelli 1999). Some researchers have argued that water and OH^- group substitution can generate two distinct iron-deficient hematite structures, commonly referred to as "protohematite" and "hydrohematite", with the general formula $Fe_{2-x/3}(OH)_xO_{3-x}$ (Wolska and Schwertmann 1989; Dang et al. 1998). The OH^- content, x, distinguishes these compounds: For $1 \leq x < 0.5$, the phase is classified as "protohematite", whereas "hydrohematite" has a lesser degree of OH^- substitution, with $0.5 \leq x < 0$. When $x = 0$, the phase is stoichiometric hematite, often abbreviated as SH in the materials sciences literature. Although "protohematite" and "hydrohematite" are not recognized by the IMA, for simplicity we will use these terms without quotations hereafter in this paper.

When hematite is precipitated from aqueous solutions under certain conditions, the reaction is thought to involve a three-stage transition sequence from protohematite to hydrohematite to stoichiometric hematite (Dang et al. 1998). Protohematite forms initially, and it exhibits the largest unit-cell volume due to structurally incorporated water. The subsequent transition to hydrohematite involves molecular water loss and a contraction of all unit-cell parameters. As structural OH^- is removed from hydrohematite and iron vacancies are filled, the *a*-axis expands as *c* continues to contract, and hydrohematite transforms to stoichiometric hematite.

During the thermal dehydration of goethite, Wolska and Schwertmann (1989) inferred that protohematite initially forms at ~250 °C based on a non-uniform broadening

of X-ray diffraction (XRD) peaks that were deemed cation dependent; these researchers attributed this broadening to the appearance of disordered iron vacancies with a concomitant substitution of OH^-. In that experiment, peak broadening ceased above 400 to 600 °C, suggesting that the iron vacancies had ordered and the structure had transitioned to hydrohematite. Stoichiometric hematite was reached at temperatures of 800 – 1050 °C.

In a separate study, Landers and Gilkes (2007) observed by transmission electron microscopy the development of micropores in synthetic hematite, and they attributed the microporosity to the loss of water from precursor protohematite and hydrohematite. Moreover, several research groups have observed a difference in the infrared (IR) and Raman spectra of stoichiometric hematite and antecedent phases (Wolska and Szajda 1985; Kustova et al. 1992; Sadykov et al. 1996; Burgina et al. 2000a; Burgina et al. 2000b). According to Burgina et al. (2000b), protohematite is identified by shifts in certain IR spectral peaks (308, 445, and 530 cm^{-1}) relative to stoichiometric hematite (333, 468, and 543 cm^{-1}). Kustova et al. (1992) and others assign additional lines in the IR spectra (3200-3500 and 900-1050 cm^{-1}) to structural OH^- groups in protohematite (Burgina et al. 2000b; Chernyshova 2007). An additional band at ~630 cm^{-1}, they assert, is due either to quasi-tetrahedral defects in the protohematite structure or to OH^- substitution (Yariv and Mendelovici 1979; Burgina et al. 2000b). Wolska and Szajda (1985) state that the ~3400, 900-950, and 630 cm^{-1} bands are characteristic of hydrohematite.

Doubts concerning protohematite and hydrohematite. Some researchers have questioned the attribution of protohematite and hydrohematite as phases distinct from

hematite. Derie et al. (1976) and Goss (1987) contend that non-uniform XRD peak broadening, additional IR peaks, and micropore formation are not indicative of intermediate phases. Instead, they argue from TEM analysis that a nonstoichiometric microporous hematite "skin" forms on the surface of goethite grains during dehydration, and this skin moves inwards during the transformation. Löffler and Mader (2006) attribute the non-uniform XRD peak broadening to nanoscale twinning in hematite, and they note that such broadening is absent in coarsely twinned hematite. Similarly, other scientists have ascribed non-uniform peak broadening to unusual behaviors with respect to particle morphology, size, microporosity, strain, and stacking faults (Watari et al. 1979a,b; Watari et al. 1983; Jiang et al. 2000; Fan et al. 2006).

Previously suggested structures for protohematite and hydrohematite. Burgina et al. (2000b) counter that morphological and defect features might possibly explain the anomalies in XRD data but not those in the IR spectra. These authors thus support the existence of hydrous hematite-like phases, and they additionally argue that the crystal structures of the precursor phases must be symmetrically different from that of hematite. Hematite is hexagonal with space group *R*-3*c* (Fig. 1). The structure contains a framework of hexagonally closest packed O^{2-} anions, and Fe^{3+} cations occupy two-thirds of the octahedral interstices (Blake and Hessevick 1966). While some proponents of the existence of protohematite and hydrohematite have assumed they share the same space group symmetry as that of stoichiometric hematite, Burgina et al. (2000b) and others have hypothesized a lower symmetry due to distortions associated with the incorporation of structural water and/or OH^- substitution in the oxygen framework (Wolska and Schwertmann 1989; Kustova et al. 1992; Sadykov et al. 1996; Gualtieri and Venturelli

1999). Burgina et al. (2000b) and Kustova et al. (1992) suggest that these distortions impose the loss of an inversion center, as the extra absorption bands in IR and Raman spectra are consistent with space group *R*3*c*. This lower symmetry would not be readily detectable using powder X-ray diffraction because *R*3*c* (C_{3v}^6) and *R*-3*c* (D_{3d}^6) exhibit the same extinction rules. However, *R*3*c* does have different selection rules than those of *R*-3*c* that can be detected with IR and Raman spectroscopies.

Crystallization of protohematite and hydrohematite. The formation of protohematite and hydrohematite is considered to be sensitive to particle size and experimental conditions (e.g., initial mineral phase, pH, solution concentrations, post-experimental treatment, etc.), and this variability may partly contribute to the ongoing controversy over their existence (Kandori et al. 1994; Burgina et al. 2000b; Pailhé et al. 2008). For example, Pailhé et al. (2008) assert that phase stability varies with the activity of water, so that crystallization differs when synthesis is performed hydrothermally rather than by dry heating (Navrotsky et al. 2008). Likewise, sample preparation methods requiring compaction and grinding of hydroxide phases such as goethite and ferrihydrite can also cause structural and chemical changes due to partial loss of water during the transformation to hematite (Sadykov et al. 1996).

As noted above, the choice of analytical technique also may contribute to the controversy over the existence of these phases. Blesa and Matijević (1989) suggest that the hydrous phases are susceptible to electron beam damage when viewed by TEM, and they argue that *ex situ* observations may fail to capture the hydrothermal crystallization sequence accurately. Ideally, the identification of protohematite and hydrohematite should be documented *in situ* and in real time using a technique that allows for time-

resolved structure refinement (Blesa and Matijević 1989; Kryukova et al. 1991; Chernyshova et al. 2007).

Here we have conducted *in situ* hydrothermal TR-XRD experiments involving the precipitation of akaganéite and its transformation to hematite, using angle-dispersive synchrotron powder X-ray diffraction coupled with Rietveld analysis. The high signal-to-noise and time resolution afforded by synchrotron XRD allowed us to capture phase transformations that are less evident when using alternative approaches. Using this technique, we argue for the existence of a lower-symmetry precursor during the crystallization of hematite in 200 ^{o}C solutions, and, for the first time, we offer a refined structure for this monoclinic phase.

EXPERIMENTAL METHODS

Sample preparation

All hydrothermal crystallization experiments were performed with solutions containing 0.45 *M* $FeCl_3$ and 0.01 *M* HCl, prepared by dilution with deionized water of a 3 *M* $FeCl_3$ stock solution made with $FeCl_3 \cdot 6H_2O$ (ACS reagent, JT Baker) and 1 *M* HCl (ACS reagent, Fisher Scientific) (Matijević and Scheiner 1978). Final solutions were passed through 0.05 μm Millipore filters and stored in sealed Nalgene bottles. For each hydrothermal precipitation experiment, ~7 μL of the 0.45 *M* $FeCl_3$ solution were loaded into 1.0 mm-outer diameter quartz glass capillaries (Charles Supper Company) and sealed with high temperature epoxy (302-3M, Epotek). Solution volumes, capillary lengths, and amount of headspace were kept as similar as possible to ensure temperature uniformity during heating and to minimize variations among samples.

207

208 **Synchrotron X-ray diffraction**

209 X-ray diffraction data of *in situ* time-resolved experiments were conducted at the
210 GeoSoilEnviroCARS (GSECARS) 13-BM-C beamline at the Advanced Photon Source
211 (APS), Argonne National Laboratory (ANL). The x-ray wavelength was 0.8265(8) Å;
212 and the detector distance was 95.165 mm. Because of low precipitate yield during *in situ*
213 experiments, capillaries were tilted at a 60° angle to allow for precipitate sedimentation to
214 the bottom of the capillary. The beam was aimed near the capillary base, enabling the
215 capture of the initial precipitation of akaganéite from solution and the phase
216 transformation to hematite. Video images of the capillary solutions revealed vigorous
217 convection of the solutions throughout the heating experiments.

218 A forced-gas heater was fabricated at APS by winding Ni coils around an inner
219 ceramic tube and applied a DC voltage using a Sorensen 33 V x 33 A (Model XHR 33-
220 33) power supply to achieve resistive heating. This assembly was encased in an outer
221 ceramic sleeve, and He gas was forced through the interior of the heated cylinder. The
222 heater was oriented normal to the capillary, and a type K chromel-alumel thermocouple
223 was situated adjacent to the capillary and monitored with a Keithly 2700 Multimeter.
224 The actual temperature was calibrated by monitoring two phase transformations of
225 $RbNO_3$ (Alfa Aesar, 99.8%, metals basis) loaded in a 1.0 mm quartz glass capillary and
226 heated from 25.7 to 250 °C. Based on this standardization, we estimate that the
227 thermocouple measured temperature was within ±1.5 °C of the actual temperature.

228 For our experiments, capillary solutions were heated to final temperatures of 150,
229 175, and 200 °C. Experimental temperatures were reached within 2 minutes and were

maintained within ±0.25 °C using the EPICS control software. TR-XRD patterns were collected every 25 to 40 seconds using a MAR165 CCD camera for run times ranging from 10 to 160 minutes. Each sample was rotated about phi (parallel to the axis of the capillary) by 1° per second during exposure. Full-circle images were integrated into intensity versus 2θ plots using the program Fit2D with a polarization factor of 0.99 (Hammersley 1996). We completed one, two, and four runs at 150, 175, and ~200 °C, respectively. The results from the experiments at 150 and 175 °C will be discussed in a separate paper.

Structure refinement

Rietveld structure refinements were performed using the EXPGUI interface of the General Structures Analysis System (GSAS) program (Toby 2001; Larson and Von Dreele 2004). The initial *R*-3*c* hematite structure parameters were taken from Blake and Hessevick (1966). Background, scale, peak profile, and unit-cell parameters were initially allowed to vary. Backgrounds were best fitted using a Chebyshev polynomial with 10 to 12 profile terms. Peak profiles were modeled using a pseudo-Voigt function described by Thompson et al. (1987) and corrected for asymmetry as described by Finger et al. (1994). After these parameters had converged, atomic positions and occupancies were refined. Soft constraints in the range of 1.90 to 2.17 Å were imposed on Fe-O bond lengths for monoclinic hydrohematite when both akaganéite and monoclinic hydrohematite phases were present. The bond restraint weighting factor was gradually reduced during the refinements. Lastly, all parameters were allowed to refine simultaneously and the weighting factor was set at one. Refining isotropic temperature factors generated

negative values, and therefore, in all TR-XRD refinements we fixed temperature factors to those determined from the hematite powder Rietveld refinement. The hematite powder was prepared from the same ferric chloride solution described above sealed in a Teflon lined bomb and heated to 150 °C in a convection oven. The 2θ range for all refinements was 15.4° to ~36° (*d*-space range: 1.3 - 3.1 Å); low angle data were removed because of the large background scattering from the capillary glass and water. After a heating run was completed and the temperature had decreased to 38 °C, a final set of XRD data were collected.

RESULTS

Akaganéite was the first phase to precipitate at all three temperatures, and in all experiments hematite was the final reaction product. Likewise, in all runs akaganéite began to precipitate before the target temperatures were reached, generally forming when the temperature surpassed ~120 °C.

A striking difference among the reactions at the three target temperatures was the reproducible appearance of split diffraction peaks when hematite crystallized in the four runs at 200 °C. These split peaks were apparent after the complete disappearance of all akaganéite peaks, but peak splitting was not observed for reactions at 150 and 175 °C (Fig. 2). The relative intensities of the component parts of the doublet hematite peaks varied slightly among the experiments at 200 °C. In one of the four runs, lower intensity "shoulders" appeared on the low 2θ side of the peaks (Fig. 2), whereas two other runs captured the emergence of shoulders on the high 2θ side (Fig. 3). A fourth experiment at 200 °C revealed a transition in peak shape (Fig. 4). During this run, the first hints of

hematite-like peaks emerged within the first 3 minutes of the experiment. After a total of 4 minutes passed, shoulders were visible on the low 2θ side as hematite crystallized, and between 6 and 6.5 minutes, the relative intensities changed and the shoulders transitioned to the high 2θ side. Between 7 and 7.5 minutes, the peaks began to merge and formed a single symmetrical peak at 8 minutes.

We attribute the variations in the behavior of the peak splitting at 200 °C to subtle differences in the heating parameters among the four runs. Despite our best efforts to maintain a uniform heating rate and target temperature, in two of our experimental runs – those that produced the shoulders on the high 2θ side – we overshot the target temperature by as much as 25 °C before it settled back to the target temperature. In contrast, in the experiments for which the target temperature was approached without significant overshooting, the doublet peaks initially appeared on the low 2θ side. We succeeded in quenching the phase with the doublet peaks by cooling in solution to 38 °C. At low temperature, the splitting was more sharply defined than at 200 °C.

DISCUSSION

The conventional space group of *R*-3*c* for stoichiometric hematite is not compatible with the peak splitting that we observed when our solutions were heated to 200 °C. We can propose two possible explanations for the peak splitting: 1) sample displacement errors, or 2) the formation of a lower symmetry hematite-like phase. We will address these possibilities in turn.

Peak splitting from sample displacement errors

Recent studies have demonstrated the sensitivity of time-resolved synchrotron XRD to certain experimental artifacts, such as peak splitting from sample displacement errors (Scarlett et al. 2010; Scarlett et al. 2011). Scarlett et al. (2011) analyzed sample displacement using capillary holders with powders deposited only as coatings on the interior walls. Because the crystals were offset from the centers of the rotating cylindrical capillaries, they yielded two characteristic displacement errors ($\pm u$). Since synchrotron radiation is so highly monochromated, the distance between opposite walls of a powder-coated capillary is sufficient to generate a splitting of all diffraction peaks. The degree of peak splitting increases with the inner-diameter of the capillary, and Scarlett et al. calculated sample displacement values based on the $\Delta 2\theta$ between split peaks; their calculated values matched the capillary diameters within error.

Because the geometry of our TR-XRD experiments so closely mirrored that used by Scarlett et al., we calculated sample displacements using $\Delta 2\theta$ for split reflections in our experiments at 200 °C and compared these values to the capillary inner diameter used in our experiments (1.0 mm) (Scarlett et al. 2011). As described in Scarlett et al. (2011) and Klug et al. (1974), a sample displacement u parallel to the incident beam in a Debye-Scherrer geometry can be expressed as follows (Fig. 5):

$$\sin\alpha = \frac{u}{R}\sin(2\theta), \qquad \text{(Eqn 1.1)}$$

where R is the detector radius, and α is the angular distance a diffracted peak is shifted from the expected peak position (O'). If crystallites precipitated as a coating on the capillary walls at points S_1 and S_2 in Figure 5, the sample would be displaced from the capillary center (O) by $\pm u$. A diffracted peak at 2θ = O' will exhibit peak position shifts

by $\pm\alpha$ to a lower (S'_1) and a higher (S'_2) angle due to equal and opposite sample displacements of 1/2 the capillary diameter:

$$S'_1 = 2\theta - \alpha,$$

$$S'_2 = 2\theta + \alpha. \quad \text{(Eqn 1.2)}$$

When we applied these relationships to our system, we calculated capillary diameters ($2u$) that ranged from 0.5 to 0.6 mm, lower than the measured values of 0.8 to 1.2 mm and the median value of 1.08 mm. We judge the disparity between the calculated and observed displacements as sufficiently large that we can discount the role of sample displacement in generating split peaks in our experiments.

Even more convincingly, our video footage of the *in situ* TR-XRD experiments strongly suggests that sample displacement did not account for the observed peak splitting. Our live image captures of the heated capillary solutions revealed that crystallization occurred primarily within the fluid and not only on capillary walls; indeed, the particles were convecting heavily at the time that peak splitting was observed. Visual inspections of capillaries after the completion of experiments likewise demonstrated that particles were not restricted to a coating on capillary walls. Finally, the absence of peak splitting in the experiments at 150 and 175 °C seems inconsistent with its attribution to an experimental artifact at 200 °C.

Peak splitting from a monoclinic hematite-like phase

Next, we consider the possibility that the observed peak splitting arose from a precursor phase with a lower symmetry than *R*-3*c* hematite. As discussed above, no such phase is recognized by the International Mineralogical Association, but previous

researchers have proposed hematite-like structures lacking a center of inversion, resulting in space group *R*3*c* (Kustova et al. 1992; Burgina et al. 2000a; Burgina et al. 2000b). However, this symmetry loss would not lead to split peaks.

In contrast, a violation of the 3-fold rotoinversion axis would diminish the symmetry from trigonal to monoclinic, and it would generate split diffraction peaks. We refined a range of low-symmetry hematite derivatives within the various subgroups of space group *R*-3*c*. Among these refinements, the highest symmetry subgroup, *I*2/*a*, was statistically no worse than the other subgroups of *R*-3*c*, including the triclinic *P*1. Thus, we developed an *I*2/*a* cell for the 200 °C refinements (Fig. 6). The unit-cell parameters were generated through the transformation of space group *R*-3*c* into *I*2/*a* using the relationship:

$$a_{mono} = 2/3a_{hex} + 4/3b_{hex} + 1/3c_{hex} \quad = 7.39 \text{ Å}$$

$$b_{mono} = a_{hex} \quad = 5.038 \text{ Å}$$

$$c_{mono} = 1/3a_{hex} + 2/3b_{hex} - 1/3c_{hex} \quad = 5.44 \text{ Å}$$

$$\beta_{mono} \quad = 95.5°$$

$$\text{Vol}_{mono} = 2/3\text{Vol}_{hex} \qquad \text{(Eqn 1.3)}$$

Atomic positions from stoichiometric hematite were mapped into the monoclinic cell using the following transformation matrix:

$$\begin{pmatrix} x_{mono} \\ y_{mono} \\ z_{mono} \end{pmatrix} = \begin{pmatrix} 0 & 1/2 & 1 \\ 1 & -1/2 & 0 \\ 0 & 1/2 & -2 \end{pmatrix} \begin{pmatrix} x_{hex} \\ y_{hex} \\ z_{hex} \end{pmatrix} \qquad \text{(Eqn 1.4)}$$

Our Rietveld refinements of the monoclinic structure represented a significant improvement over the refinements using a trigonal space group. Representative *I*2/*a* and *R*-3*c* Rietveld refinement results are presented in Figures 7 and 8. Space group *I*2/*a*

provided a better fit and lower χ^2 (0.639_{mono} vs. 2.721_{hex}), R_{wp} (0.0099_{mono} vs. 0.0205_{hex}), and $R(F^2)$ (0.0115_{mono} vs. 0.0175_{hex}) values relative to *R*-3*c*. Moreover, the final monoclinic structure seems reasonable with respect to interatomic bond distances and angles, and all reflections produced by a structure with this space group symmetry were consistent with the data. Final refinement parameters, atomic coordinates, and selected bond lengths are compiled in Tables 1, 2, and 3.

We searched the literature for X_2O_3 analogs and found a V_2O_3 phase that undergoes a transition to a monoclinic (*I*2/*a*) structure as a function of temperature (Dernier and Marezio 1970; McWhan and Remeika 1970). *R*-3*c* V_2O_3 experiences a monoclinic distortion below 160 K, at which point it becomes isostructural with our monoclinic hematite-like phase. During the V_2O_3 *R*-3*c* to *I*2/*a* transition, vanadium-vanadium pairs rotate by 1.8° in the a_{mono} - c_{mono} plane (Dernier and Marezio 1970). A similar distortion takes place during the formation of hydrohematite, where the equivalent iron-iron pairs rotate by ~1.6°.

We note that Bora et al. (2012) have observed and described peak splitting in XRD analyses of hematite nanoparticles that were heat treated from 250 to 900 ^{o}C in air. Specifically, these authors report that diffraction peaks remained constant in shape and position up to 650 ^{o}C, but from 700 to 900 ^{o}C the broad peaks resolved into distinctly split peaks (see Figure 2B in that paper). They speculate that the splitting might be due to a distortion of the hexagonal structure (as we do here) or to compressive stress on the nanocrystalline surface in response to increased oxygen content with higher temperature. Because these authors used conventional Cu$K\alpha$ radiation, however, it is not clear whether the splitting that they report represents the same phenomenon that we observed, or

whether the effect is due to a sharpening of the initially broad peaks during higher temperature annealing, thereby allowing the $K\alpha_1$ and $K\alpha_2$ components to become distinct. The use of monochromatic synchrotron radiation in the present study rules out that possibility as a cause of the splitting that we report.

In situ formation of hydrohematite

We interpret the monoclinic hematite-like phase in our experiments as a variety of "hydrohematite", in the sense that Wolska and Schwertmann (1989) and Dang et al. (1998) define the term. We base this assertion on three factors: 1) the similarity of our refined monoclinic phase to structures that other researchers have posited for hydrohematite; 2) the increase in our refined octahedral Fe occupancies in hydrohematite during its conversion to stoichiometric hematite; 3) the behavior of the lattice parameters of hydrohematite as the reaction progressed. We note that our XRD experiments did not reveal evidence of symmetrically distinct "protohematite" and "hydrohematite" phases, and so we simply call the intermediate phase hydrohematite.

Similarity to prior models of hydrohematite. The structure of stoichiometric hematite contains sets of two face-sharing, trigonally distorted octahedra forming chains along the *c* axis that are separated by vacancies, resulting in one unshared face per octahedron (Fig. 1 and 9) (Blake and Hessevick 1966). Each octahedron shares 3 edges and 6 corners with neighboring octahedra. Each octahedron consists of three longer Fe-O face-sharing bond lengths (2.116 Å) and three shorter unshared Fe-O bond lengths (1.945 Å) (Blake and Hessevick 1966). Iron atoms are displaced from octahedral centers and shift towards vacancies due to electrostatic repulsion between face-sharing octahedra. Fe-

Fe distances (2.900 Å) between face sharing octahedra along *c* are longer than edge sharing octahedral Fe-Fe distances (2.971 Å) within the octahedral layers.

According to Burgina et al. (2000b), hexagonal protohematite/hydrohematite Fe-O bond lengths deviate from the ideal stoichiometric hematite because OH^- is "substituting" for oxygen. As a result, face-sharing Fe-O bond lengths increase (2.18 Å), while edge-sharing Fe-O bond lengths contract (1.90 Å). The Fe-Fe face-sharing and neighboring distances remain essentially unaltered. Because OH^- substitution affects the O framework, the shifts in oxygen positions eliminate the center of inversion of *R*-3*c* (Sadykov et al. 1996; Burgina et al. 2000a; Burgina et al 2000b).

Our refined structure for monoclinic hydrohematite revealed distortions that are compatible with H incorporation. The refined Fe-O bond lengths varied between 1.855(15) and 2.19(15) Å, which are similar to previously reported hydrohematite Fe-O bond lengths. Face sharing Fe-Fe distances remained approximately the same as those for stoichiometric hematite and hydrohematite (2.8830(21) Å), but neighboring Fe-Fe distances ranged from 2.906(7) to 3.028(10) Å. All bond length and distance averages were approximately the same as the values reported by Blake and Hessevick (1966). However, the Fe-O bond length and Fe-Fe distance variations due to OH^- substitution produce a significant structural distortion to the octahedra. The distortion manifests as a ~1.6° tilt of Fe-Fe pairs in the a_{mono} - c_{mono} plane, effectively removing the 3-fold rotoinversion axis. This canting of the Fe-Fe pairs occurs in the opposite sense as occurs in V_2O_3. In V_2O_3, the V-V tilt displaces the V cations towards the vacancies, whereas in hydrohematite the Fe-Fe tilt moves the Fe cations away from the vacant sites, consistent with a model in which H cations are bonded to O anions that neighbor vacancies.

436 **Decrease in octahedral Fe occupancy.** Our refinement of the first monoclinic
437 hydrohematite phases to crystallize in our experiments revealed non-unitary Fe
438 occupancies, as low as 0.72(6) in one of our runs. The oxygen site occupancies refined as
439 unity. Moreover, we observed an increase in the refined Fe occupancy to a final value of
440 0.980(6) within 2.5 minutes after the first appearance of hematite (Fig. 10). In contrast,
441 our refinements of the stoichiometric hematite final products consistently yielded
442 octahedral sites that were fully occupied by Fe.

443 Wolska and Schwertmann (1989) and others predict that hydrohematite contains
444 Fe vacancies in order to maintain charge balance from the OH^- substitution for O^{2-}
445 (Wolska and Schwertmann 1989; Dang et al. 1998; Gualtieri and Venturelli 1999;
446 Burgina et al. 2000a; Burgina et al. 2000b; Chernyshova et al. 2007). Assuming that OH^-
447 substitution is accommodated solely by Fe vacancies, Wolska (1981) notes that the
448 weight percent water within hydrohematite can be calculated from the absent iron using
449 the relation

450 $$x = \frac{(9.07y)}{(51.15+y)} \qquad \text{(Eqn 1.5)}$$

451 where y is the weight % of water within the structure and x represents the substitutional
452 OH^- in the formula $Fe_{2-x/3}(OH)_xO_{3-x}$. Our refined Fe occupancy of 0.73 for the incipient
453 hydrohematite in our experiments yields a water content of 11.63 wt%, which is similar
454 to the water concentration observed in familiar FeOOH phases, such as goethite (10.14
455 wt% H_2O) and akaganéite (11.48 wt% H_2O) (Post and Buchwald 1991; Cornell and
456 Schwertmann 2001; Post et al. 2003). Thus, the transition from akaganéite to the first
457 hydrohematite crystals that formed in our experiments apparently involved no water loss,
458 suggesting that the hydrothermal transformation of akaganéite to hydrohematite is

459 promoted not by dehydration but by a thermodynamically driven framework
460 reconstruction. Moreover, this analysis reveals that defect hematite phases are capable of
461 storing large quantities of water.

462 **Variations in lattice parameters.** As suggested by Dang et al. (1998), the
463 reaction from protohematite to hydrohematite to stoichiometric hematite is best captured
464 through characteristic trends in unit-cell parameters. The protohematite to hydrohematite
465 transition occurs through isotropic contraction, whereas the transformation from
466 hydrohematite to stoichiometric hematite involves the selective expansion of the *a*-axis.

467 Our experiments showed similar trends, explaining the surprising shift of peak
468 shoulders from the low to the high 2θ side of the "primary" peaks as crystallization
469 progressed (Fig. 4 and 11). The appearance of shoulders on the low 2θ sides of peaks is
470 attributable to the co-contraction of the pseudo-hexagonal *a*- and *c*-axes ("protohematite"
471 stage). As the *c*-axis continued to contract and as the *a*-axis expanded, shoulders moved
472 to the high-angle sides of the peaks ("hydrohematite" stage). In the final step, *c* expanded
473 and *a* contracted, and the peaks became symmetric (yielding stoichiometric *R*-3*c*
474 hematite).

475 **Conditions of hydrohematite formation.** The absence of peak splitting in our
476 lower-temperature experiments seems counter-intuitive, since our Rietveld analyses of
477 the incipient hematite crystals that formed during the experiments at 150 and 175 ^{o}C also
478 indicated Fe vacancies on the order of 25%. We suggest that reaction kinetics likely play
479 an important role in the formation of the monoclinic variety of hydrohematite. Hummer
480 et al. (2013) have argued that the hydration of mineral surfaces is more effective at low
481 than at high temperatures. Since hydration can decrease distortions of surface structure,

high temperatures actually may better promote departures from structural ideality at nanoparticle surfaces. Moreover, we infer that the distortion of the O framework in hydrohematite also is tied to the rapidity of crystallization at higher temperatures. The controlling role of kinetics over thermodynamics occurs in other hydrothermal systems at high rather than low temperatures. For instance, Brand et al. (2012) report that a mixture of rhombohedral and monoclinic potassium jarosites form under hydrothermal conditions at 120 °C, but only the stable rhombohedral phase crystallizes at 80 °C.

Finally, like Chernyshova et al. (2007), we emphasize that aqueous environments obviously are important in stabilizing intermediate hydrous hematite phases. Indeed, in a previous study, our group monitored the formation of hematite during the dry-heating of akaganéite from 26 to 800 °C (Post et al. 2003). Akaganéite started to transform to hematite at ~300 °C, and our re-examination of those X-ray diffraction patterns at the transition revealed no evidence for split hematite peaks.

IMPLICATIONS

Our *in situ* hydrothermal XRD experiments at 200 °C enabled us to capture the formation of hydrous precursors to hematite, supporting claims for the existence of "hydrohematite" phases that go back more than 150 years. The formation of monoclinic hydrohematite and its incorporation of OH^- have important geological and industrial implications. For example, hematite experiences a magnetic transition at ~260 K, known as the Morin transition temperature, T_M. The T_M and the temperature range over which the transition takes place (ΔT_M) are highly dependent on factors such as particle size, crystallinity, and OH^- substitution. Since the Morin temperature varies from sample to

505 sample, its value can provide insight into the conditions under which natural hematite
506 forms (Dang et al. 1998; Zboril et al. 2002; Bengoa et al. 2010; Fleischer et al. 2010; Liu
507 et al. 2010).

508 Similarly, the chemical properties of hematite depend strongly on its hydration
509 state. Burgina et al. (2000b) report that the catalytic activity of protohematite is 10 times
510 greater than that for stoichiometric hematite. Jang et al. (2007) have demonstrated that
511 the dissolution rate of hematite increases with greater structural disorder. The degree of
512 distortion of Fe octahedra, and thus the change in symmetry due to the incorporation of
513 OH^-, will also impact the physical properties of hematite. For example, Pailhé et al.
514 (2008) observed that the color of hematite particles can be tuned by controlling the
515 degree of distortion of Fe octahedra. By extension, particle characteristics of hematite
516 used in prehistoric paints might help us determine whether the hematite was formed
517 naturally or purposely produced as a red pigment (Salomon et al. 2012).

518 Finally, hematite is considered a significant component of the Martian regolith,
519 and the presence of hydrohematite may yield information about the depositional history
520 of Martian soils. For example, Golden et al. (2008) speculate that deposits of hematite
521 spherules on Mars formed via a hydrohematite intermediate by aging under hydrothermal
522 conditions. As our XRD results reveal that hydrohematite can store surprisingly large
523 concentrations of water within its structures, this phase may serve as an unappreciated
524 reservoir of water on Mars.

525

526

527

ACKNOWLEDGMENTS

This work was made possible by the National Science Foundation grants EAR07-45374 and EAR11-47728 and the Center for Environmental Kinetics Analysis (CEKA), an NSF- and DOE-sponsored Environmental Molecular Sciences Institute (CHE-0431328). GeoSoilEnviroCARS is supported by the National Science Foundation - Earth Sciences (EAR-1128799) and Department of Energy - Geosciences (DE-FG02-94ER14466). The Advanced Photon Source is supported by the U.S. Department of Energy, Office of Science, Basic Energy Sciences, under Contract No. W-31-109-Eng-38. We thank Joanne Stubbs and Nancy Lazarz at GSECARS BM-13, as well as Tim Fisher for their invaluable assistance in data collection at the beamline.

REFERENCES

Bengoa, J.F., Alvarez, A.M., Bianchi, A.E., Punte, G., Vandenberghe, R.E., Mercader, R.C., and Marchetti, S.G. (2010) The Morin transition in nanostructured pseudocubic hematite: Effect of the intercrystallite magnetic exchange. Materials Chemistry and Physics, 123, 191-198.

Blake, R.L. and Hessevick, R.E. (1966) Refinement of hematite structure. American Mineralogist, 51, 123-129.

Blesa, M.A. and Matijević, E. (1989) Phase transformations of iron oxides, oxohydroxides, and hydrous oxides in aqueous media. Advances in Colloid and Interface Science, 29, 173-221.

Boyd, P.W. and Ellwood, M.J. (2010) The biogeochemical cycle of iron in the ocean. Nature Geoscience, 3, 675-682.

Bora, D.K., Braun, A., Erat, S., Safonova, O., Graule, T., and Constable, E.C. (2012) Evolution of structural properties of iron oxide nano particles during temperature treatment from 250 ^{o}C to 900 ^{o}C: X-ray diffraction and Fe K-shell pre-edge X-ray absorption study. Current Applied Physics, 12, 817-825.

Brand, H.E.A., Scarlett, N.V.Y., and Grey, I.E. (2012) In situ studies into the formation kinetics of potassium jarosite. Journal of Applied Crystallography, 45, 535-545.

Breithaupt, A. (1847) Vollständiges Handbuch der Mineralogie. Arnoldische Buchhandlung, Dresden.

559 Brush, G.J and Rodman, C.S. (1867) Observations on the native hydrates of iron.
560 American Journal of Science and Arts, 44, 219-222.

561 Burgina, E.B., Kustova, G.N., Isupova, L.A., Tsybulya, S.V., Kryukova, G.N., and
562 Sadykov, V.A. (2000a) Investigation of the structure of protohematite—metastable
563 phase of ferrum (III) oxide. Journal of Molecular Catalysis A: Chemical, 158, 257-
564 261.

565 Burgina, E.B., Kustova, G.N., Tsybulya, S.V., Kryukova, G.N., Litvak, G.S., Isupova,
566 L.A., and Sadykov, V.A. (2000b) Structure of the metastable modification of iron
567 (III) oxide. Journal of Structural Chemistry, 41, 396-402.

568 Cheng, W., He, J., Sun, Z., Peng, Y., Yao, T., Liu, Q., Jiang, Y., Hu, F., Xie, Z., He, B.,
569 and Wei, S. (2012) Ni-doped overlayer hematite nanotube: A highly photoactive
570 architecture for utilization of visible light. The Journal of Physical Chemistry C,
571 116, 24060-24067.

572 Chernyshova, I.V., Hochella, J., M F, and Madden, A.S. (2007) Size-dependent structural
573 transformations of hematite nanoparticles. 1. Phase transition. Physical Chemistry
574 Chemical Physics, 9, 1736.

575 Chernyshova, I.V., Ponnurangam, S., and Somasundaran, P. (2010) On the origin of an
576 unusual dependence of (bio)chemical reactivity of ferric hydroxides on nanoparticle
577 size. Physical Chemistry Chemical Physics, 12, 14045.

578 Christensen, P.R. (2004) Formation of the hematite-bearing unit in Meridiani Planum:
579 Evidence for deposition in standing water. Journal of Geophysical Research, 109,

E08003.

Cornell, R.M., Schwertmann, U., Cornell, R.M., and Schwertmann, U. (2001) The Iron Oxides: Structure, Properties, Reactions, Occurrences and Uses. Wiley-VCH.

Dana, J.D. and Brush, G.J. (1868) A System of Mineralogy, 5th Ed. Wiley and Son, New York.

Dang, M.Z., Rancourt, D.G., Dutrizac, J.E., Lamarche, G., and Provencher, R. (1998) Interplay of surface conditions, particle size, stoichiometry, cell parameters, and magnetism in synthetic hematite-like materials. Hyperfine Interactions, 117, 271-319.

Derie, R., Ghodsi, M., and Calvo-Roche, C. (1976) DTA study of the dehydration of synthetic goethite αFeOOH. Journal of Thermal Analysis and Calorimetry, 9, 435-440.

Dernier, P.D., and Marezio, M. (1970) Crystal structure of the low-temperature antiferromagnetic phase of V2O3. Physical Review B, 2, 3771.

Fan, H., Song, B., and Li, Q. (2006) Thermal behavior of goethite during transformation to hematite. Materials chemistry and physics, 98, 148-153.

Finger, L.W., Cox, D.E., and Jephcoat, A.P. (1994) A correction for powder diffraction peak asymmetry due to axial divergence. Journal of Applied Crystallography, 27, 892-900.

Fleischer I., Agresti, D.G., Klingelhöfer, G., and Morris, R.V. (2010) Distinct hematite

populations from simultaneous fitting of Mössbauer spectra from Meridiani Planum, Mars. Journal of Geophysical Research, 115, E00F06.

Gialanella, S., Belli, R., Dalmeri, G., Lonardelli, I., Mattarelli, M., Montagna, M., and Toniutti, L. (2011) Artificial or natural origin Of hematite-based red pigments in archaeological contexts: The case of Riparo Dalmeri (Trento, Italy). Archaeometry, 53, 950-962.

Glotch, T.D. (2004) Effect of precursor mineralogy on the thermal infrared emission spectra of hematite: Application to Martian hematite mineralization. Journal of Geophysical Research, 109, E07003.

Glotch, T.D. and Kraft, M.D. (2008) Thermal transformations of akaganéite and lepidocrocite to hematite: assessment of possible precursors to Martian crystalline hematite. Physics and Chemistry of Minerals, 35, 569-581.

Golden, D.C., Ming, D.W., Morris, R.V., and Graff, T.G. (2008) Hydrothermal synthesis of hematite spherules and jarosite: Implications for diagenesis and hematite spherule formation in sulfate outcrops at Meridiani Planum, Mars. American Mineralogist, 93, 1201-1214.

Goss, C.J. (1987) The kinetics and reaction mechanism of the goethite to hematite transformation. Mineralogical Magazine, 51, 437-451.

Gualtieri, A.F., and Venturelli, P. (1999) In situ study of the goethite-hematite phase transformation by real time synchrotron powder diffraction. American Mineralogist, 84, 895-904.

621 Hammersley, A.P. (1996) Two-dimensional detector software: From real detector to
622 idealized image or two-theta scan. High Pressure Research, 14, 235.

623 Hermann, R. (1844) Untersuchungen russischer Mineralien. Journal fur Praktische
624 Chemie, 33, 87-98.

625 Hummer, D.R., Kubicki, J.D., Kent, P.R.C., and Heaney, P.J. (2013) Single-site and
626 monolayer surface hydration energy of anatase and rutile nanoparticles using
627 density functional theory. Journal of Physical Chemistry B, 49, 26,084-26,090.

628 Hüttig, G.F., and Strotzer, E. (1936) Die aktiven Zustände, welche im Verlaufe der
629 Zersetzung des Nadeleisenerzes in α•Eisenoxyd und Wasserdampf durchschritten
630 werden (Aktive Oxyde. Mitteilung). Zeitschrift für Anorganische und Allgemeine
631 Chemie, 226, 97-125.

632 Jang, J.H., Dempsey, B.A., and Burgos, W.D. (2007) Solubility of hematite revisited:
633 Effects of hydration. Environmental Science & Technology, 41, 7303-7308.

634 Jia, C., Cheng, Y., Bao, F., Chen, D., and Wang, Y. (2006) pH value-dependant growth
635 of α-Fe2O3 hierarchical nanostructures. Journal of Crystal Growth, 294, 353-357.

636 Jiang, J.Z., Ståhl, K., Nielsen, K., and Da Costa, G.M. (2000) Anisotropic x-ray line
637 broadening in goethite-derived haematite. Journal of Physics: Condensed Matter,
638 12, 4893.

639 Kandori, K., Ohnishi, S., Fukusumi, M., and Morisada, Y. (2008) Effects of anions on the
640 morphology and structure of hematite particles produced from forced hydrolysis of

641 Fe(NO3)3–HNO3. Colloids and Surfaces A: Physicochemical and Engineering
642 Aspects, 331, 232-238.

643 Kandori, K., Tamura, S., and Ishikawa, T. (1994) Inner structure and properties of
644 diamond-shaped and spherical α-Fe2O3 particles. Colloid and Polymer Science, 27,
645 812-819.

646 Killebrew, J.B. (1879) Middle Tennessee as an Iron Centre. Tavel, Eastman, and
647 Howell, Nashville, TN.

648 Klug, H.P., and Alexander, L.E. (1974) X-ray diffraction procedures for polycrystalline
649 and amorphous materials. 966 p. Wiley-Interscience.

650 Kryukova, G.N., Tsybulya, S.V., Solovyeva, L.P., Sadykov, V.A., Litvak, G.S., and
651 Andrianova, M.P. (1991) Effect of heat treatment on microstructure evolution of
652 haematite derived from synthetic goethite. Materials Science and Engineering: A,
653 149, 121-127.

654 Kurnakow, N.S. and Rode, E.J. (1928) Chemische konstitution der natürlichen
655 eisenoxydhydrate. Zeitschrift für Anorganische und Allgemeine Chemie, 169, 57-
656 80.

657 Kustova, G.N., Burgina, E.B., Sadykov, V.A., and Poryvaev, S.G. (1992) Vibrational
658 spectroscopic investigation of the goethite thermal decomposition products. Physics
659 and Chemistry of Minerals, 18, 379-382.

660 Landers, M. and Gilkes, R. (2007) Dehydroxylation and dissolution of nickeliferous

goethite in New Caledonian lateritic Ni ore. Applied Clay Science, 35, 162-172.

Larson, A.C., and Von Dreele, R.B. (2004) General Structure Analysis System (GSAS).

Liu, X., Zhang, J., Guo, X., Wu, S., and Wang, S. (2010) Porous α-Fe2O3 decorated by Au nanoparticles and their enhanced sensor performance. Nanotechnology, 21, 095501.

Löffler, L., and Mader, W. (2006) Anisotropic X-ray peak broadening and twin formation in hematite derived from natural and synthetic goethite. Journal of the European Ceramic Society, 26, 131-139.

Lu, B., Guo, H., Li, P., Liu, H., Wei, Y., and Hou, D. (2011) Comparison study on transformation of iron oxyhydroxides: Based on theoretical and experimental data. Journal of Solid State Chemistry, 184, 2139-2144.

Matijević, E. and Scheiner, P. (1978) Ferric hydrous oxide sols: III. Preparation of uniform particles by hydrolysis of Fe (III)-chloride, -nitrate, and -perchlorate solutions. Journal of Colloid and Interface Science, 63, 509-524.

McWhan, D.B. and Remeika, J.P. (1970) Metal-Insulator Transition in V(1-x)Cr(x)2O3. Physical Review B, 2, 3734.

Navrotsky, A., Mazeina, L., and Majzlan, J. (2008) Size-driven structural and thermodynamic complexity in iron oxides. Science, 319, 1635-1638.

Nickel, E.H. and Nichols, M.C. (1991) Mineral Reference Manual. Van Nostrand Reinhold, New York.

Pailhé, N., Wattiaux, A., Gaudon, M., and Demourgues, A. (2008) Impact of structural features on pigment properties of α-Fe2O3 haematite. Journal of Solid State Chemistry, 181, 2697-2704.

Palache, C., Berman, H., and Frondel, C. (1944) The System of Mineralogy of James Dwight Dana and Edward Salisbury Dana, 7th Ed. Wiley, New York.

Posnjak, E. and Merwin, H.E. The hydrated ferric oxides. American Journal of Science, 47, 311-347.

Post, J.E. and Buchwald, V.F. (1991) Crystal structure refinement of akaganéite. American Mineralogist, 76, 272-277.

Post, J.E., Heaney, P.J., Von Dreele, R.B., and Hanson, J.C. (2003) Neutron and temperature-resolved synchrotron X-ray powder diffraction study of akaganéite. American Mineralogist, 88, 782-788.

Potter, S.L., Chan, M.A., Petersen, E.U., Dyar, M.D., and Sklute, E. (2011) Characterization of Navajo Sandstone concretions: Mars comparison and criteria for distinguishing diagenetic origins. Earth and Planetary Science Letters, 301, 444-456.

Sadykov, V.A., Isupova, L.A., Tsybulya, S.V., Cherepanova, S.V., Litvak, G.S., Burgina, E.B., Kustova, G.N., Kolomiichuk, V.N., Ivanov, V.P., and Paukshtis, E.A. (1996) Effect of mechanical activation on the real structure and reactivity of iron (III) oxide with corundum-type structure. Journal of Solid State Chemistry, 123, 191-202.

Salomon, H., Vignaud, C., Coquinot, Y., Beck, L., Stringer, C., Strivay, D., and D'errico, F. (2012) Selection and heating of colouring materials in the Mousterian level of Es-Skhul *(c.* 100,000 Years BP, Mount Carmel, Israel). Archaeometry, 54, 698-722.

Scarlett, N.V.Y., Grey, I.E., and Brand, H.E.A. (2010) Ordering of iron vacancies in monoclinic jarosites. American Mineralogist, 95, 1590-1593.

Scarlett, N.V.Y., Rowles, M.R., Wallwork, K.S., and Madsen, I.C. (2011) Sample-displacement correction for whole-pattern profile fitting of powder diffraction data collected in capillary geometry. Journal of Applied Crystallography, 44, 60-64.

Shanker, U., Bhushan, B., Bhattacharjee, G., and Kamaluddin. (2011) Formation of nucleobases from formamide in the presence of iron oxides: implication in chemical evolution and origin of life. Astrobiology, 11, 225-233.

Spencer, L.J. (1919) Mineralogical characters of turite (=turgite) and some other iron-ores from Nova Scotia. Mineralogical Magazine, 18, 339-348.

Thompson, P., Cox, D.E., and Hastings, J.B. (1987) Rietveld refinement of Debye-Scherrer synchrotron X-ray data from Al2O3. Journal of Applied Crystallography, 20, 79-83.

Toby, B.H. (2001) EXPGUI, a graphical user interface for GSAS. Journal of Applied Crystallography, 34, 1-4.

Watari, F., Van Landuyt, J., Delavignette, P., and Amelinckx, S. (1979a) Electron

microscopic study of dehydration transformations. I. Twin formation and mosaic structure in hematite derived from goethite. Journal of Solid State Chemistry, 29, 137-150.

Watari, F., Delavignette, P., and Amelinckx, S. (1979b) Electron microscopic study of dehydration transformations. II. The formation of "superstructures" on the dehydration of goethite and diaspore. Journal of Solid State Chemistry, 29, 417-427.

Watari, F., Delavignette, P., Van Landuty, J., and Amelinckx, S. (1983) Electron microscopic study of dehydration transformations. Part III: High resolution observation of the reaction process FeOOH→ Fe2O3. Journal of Solid State Chemistry, 48, 49-64.

Wolska, E. (1981) The structure of hydrohematite. Zeitschrift für Kristallographie, 154, 69-75.

Wolska, E. (1988) Relations between the existence of hydroxyl ions in the anionic sublattice of hematite and its infrared and X-ray characteristics. Solid State Ionics, 28, 1349-1351.

Wolska, E., and Schwertmann, U. (1989) Nonstoichiometric structures during dehydroxylation of goethite. Zeitschrift für Kristallographie, 189, 223-237.

Wolska, E., and Szajda, W. (1985) Structural and spectroscopic characteristics of synthetic hydrohaematite. Journal of Materials Science, 20, 4407-4412.

742 Yanina, S.V., and Rosso, K.M. (2008) Linked reactivity at mineral-water interfaces
743 through bulk crystal nonduction. Science, 320, 218-222.

744 Yariv, S., and Mendelovici, E. (1979) Effect of degree of crystallinity on the infrared-
745 spectrum of hematite. Applied Spectroscopy, 33, 410-411.

746 Zboril, R., Mashlan, M., and Petridis, D. (2002) Iron(III) Oxides from thermal processes
747 synthesis, structural and magnetic properties, Mössbauer spectroscopy
748 characterization, and applications. Chemistry of Materials, 14, 969-982.

749

Tables

Table 1. Final unit cell parameters and refinement results for space groups *I*2/*a* and *R*-3*c* at 38 °C

Space group	*I*2/*a*	*R*-3*c*
	Unit cell	
a (Å)	7.3951(10)	5.0297(5)
b (Å)	5.0117(5)	5.0297(5)
c (Å)	5.4417(7)	13.7502(18)
α (°)	90	90
β (°)	95.666(5)	90
γ (°)	90	120
V (Å^3)	200.70(6)	301.24(8)
	Refinement	
No. of data points	1031	1031
No. of reflections	54	19
Diffraction range (*d* Å)	15.4-36.01	15.4-36.05
No. of variables	30	22
$R(F^2)$	0.0115	0.0175
R_{wp}	0.0099	0.0205
χ^2	0.639	2.721

Table 2. Atomic coordinates, site occupancies, and isotropic displacement values for space group *I*2/*a* at 38 °C

Atom	*x*	*y*	*z*	Site occupancy factor	U_{iso}
Fe1	0.3589(4)	-0.0043(11)	0.2944(4)	0.973(6)	0.004
O1	0.4117(21)	0.8579(27)	0.6327(29)	1.0	0.007
O2	0.25	0.183(4)	0	1.0	0.007

Table 3. Selected bond lengths for space group *I*2/*a* at 38 °C (Å)

Within one octahedron		Intralayer		Interlayer	
Fe1-O1	2.033(20)	Fe1-Fe2	2.906(7)	Fe2-Fe7[b]	2.8830(21)
Fe1-O2	1.960(8)	Fe2-Fe3	2.956(10)		
Fe1-O3	1.855(16)	Fe1-Fe6	3.028(10)		
<Fe-O>[c]	1.949	<Fe-Fe>[a]	2.963		
Fe1-O4	1.969(17)	O1-O2	3.022(26)		
Fe1-O5	2.190(15)	O1-O3	3.047(12)		
Fe1-O6	2.161(15)	O2-O3	3.051(10)		
<Fe-O>[d]	2.107	<O-O>[g]	3.04		
O1-O4	2.928(10)	O4-O5	2.669(23)		
O2-O5	2.925(21)	O4-O6	2.659(16)		
O3-O6	2.811(20)	O5-O6	2.659(16)		
<O-O>[e]	2.888	<O-O>[h]	2.662		
O1-O5	3.02(4)				
O2-O6	2.802(9)				
O3-O4	2.49(4)				
<O-O>[f]	2.771				

Values from Blake (1966): (a) 2.971, (b) 2.9, (c) 1.945, (d) 2.116, (e) 2.888, (f) 2.773, (g) 3.035, (h) 2.669 in Å
Labels for Fe and O atoms correspond to Figure 9

Figures

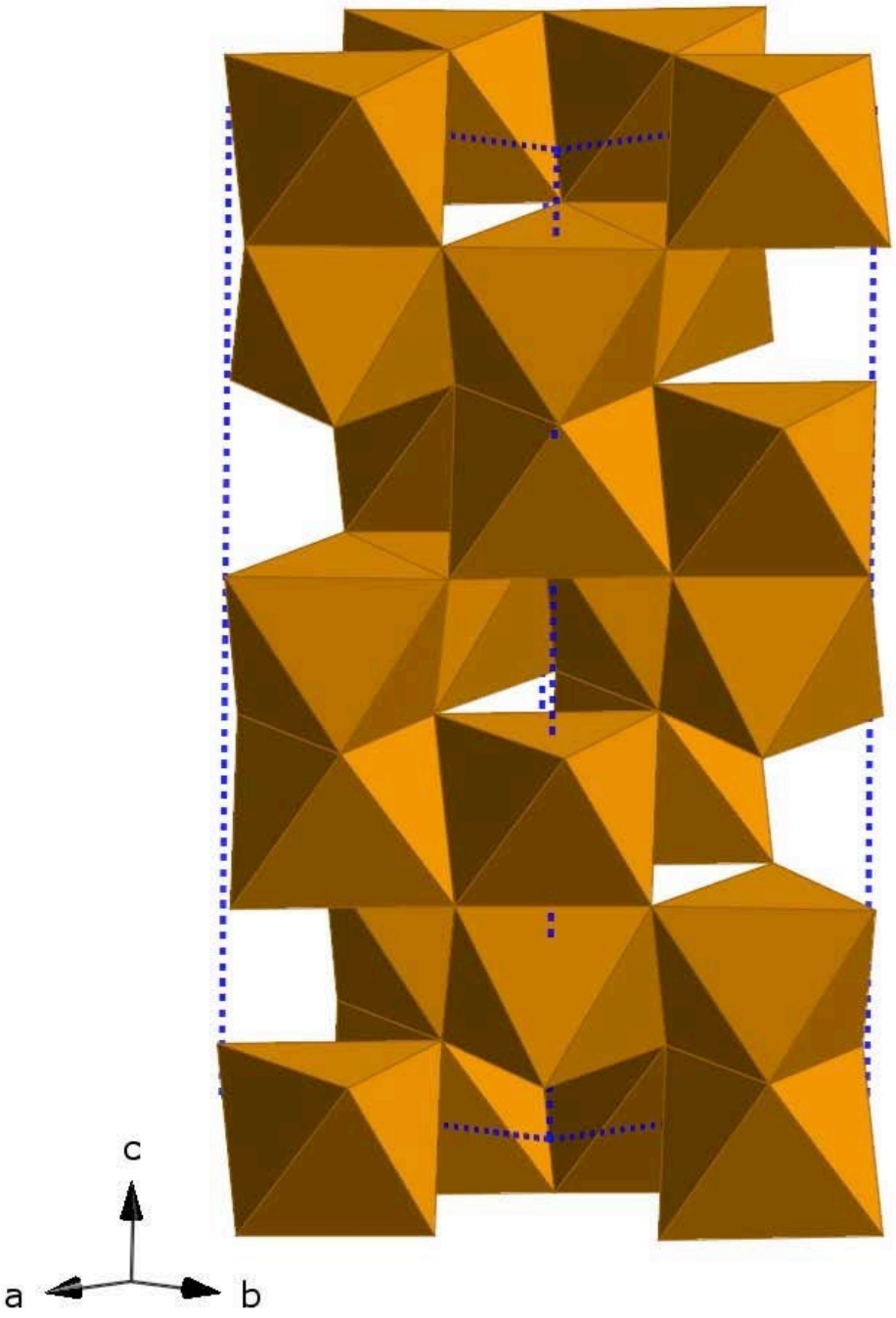

Figure 1. Crystal structure of hematite in the hexagonal setting (*R*-3*c*).

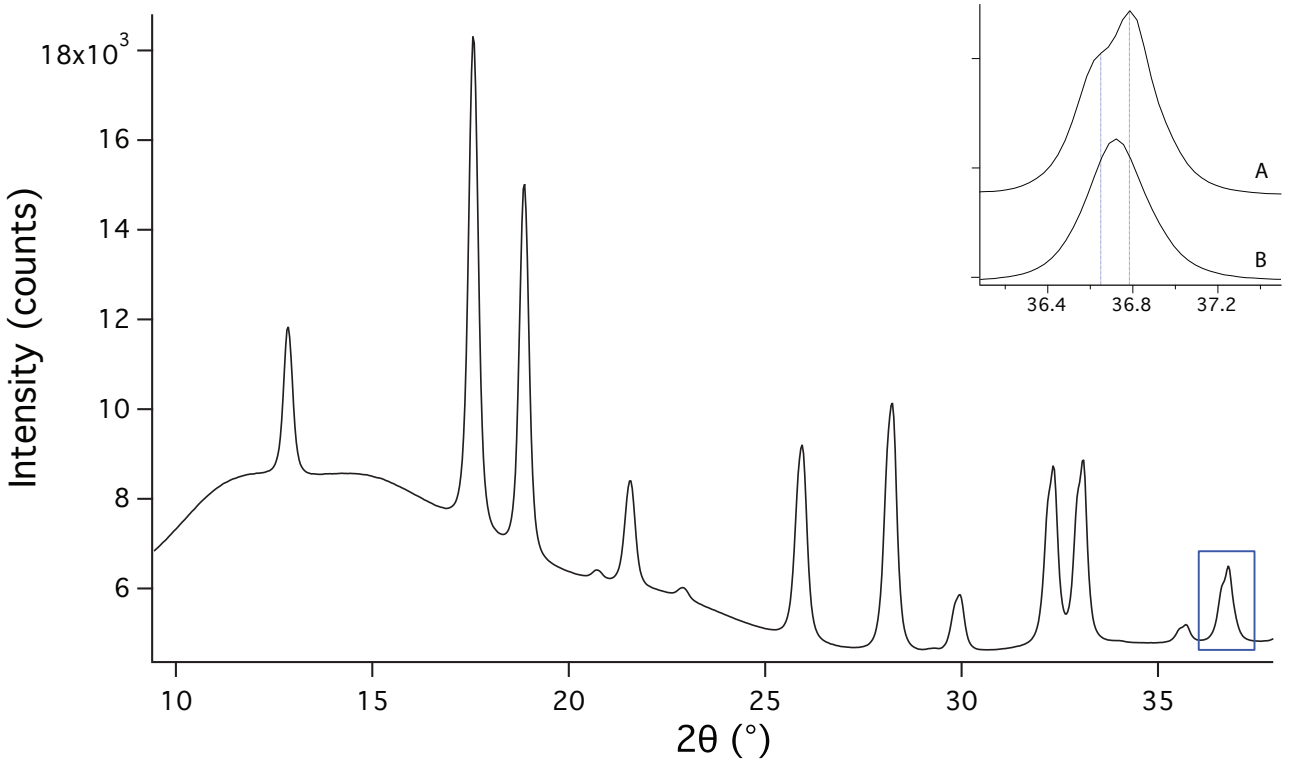

Figure 2. Peak splitting in a hematite X-ray diffraction pattern from experiment 1. Shoulders are on the low 2θ side (A). Standard *R*-3*c* hematite diffraction patterns do not display peak splitting (B).

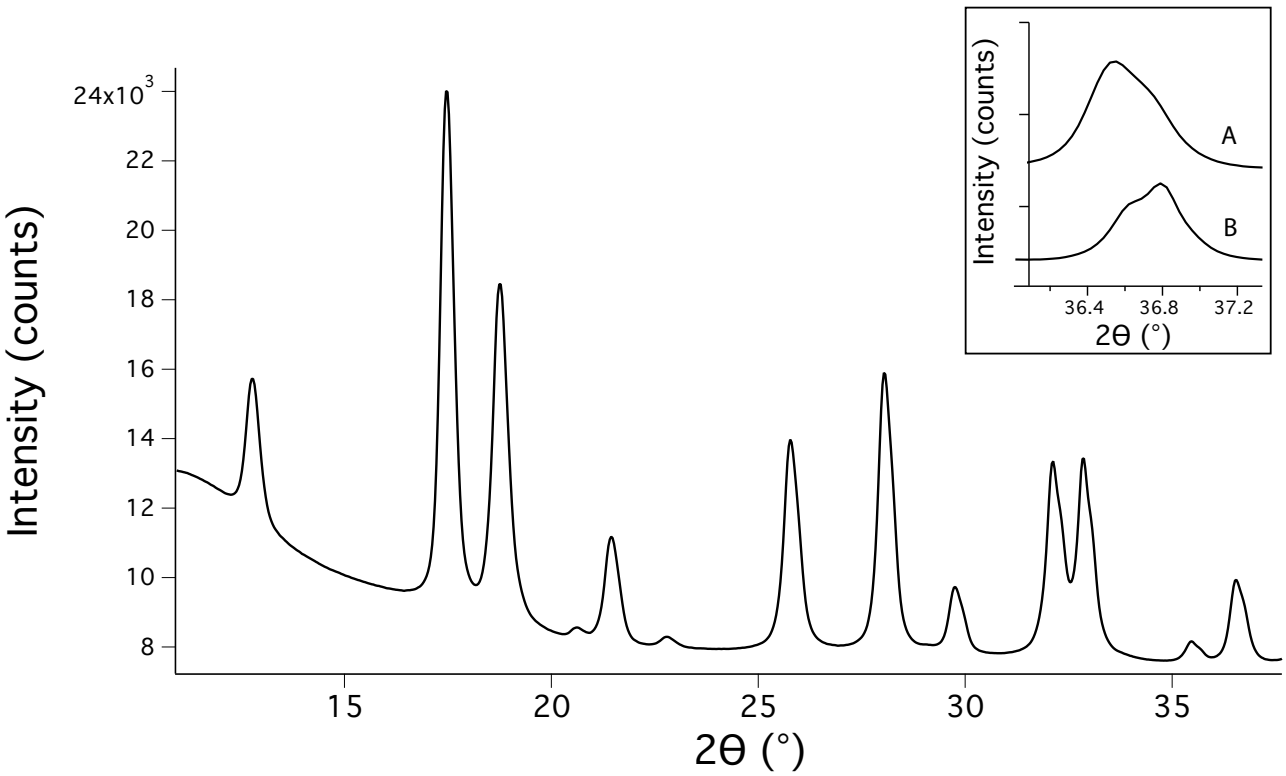

Figure 3. Peak splitting in a hematite X-ray diffraction pattern from experiment 3. Experiment 3 shoulders are on the high 2θ side, while experiment 1 shoulders are on the low 2θ side.

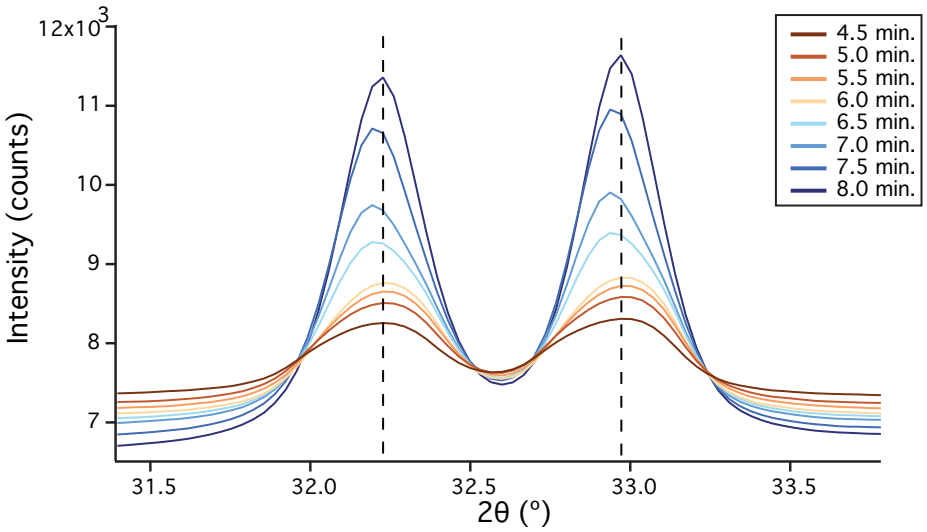

Figure 4. Time series of diffraction patterns of experiment 2 at 200 °C from 4.5 to 8 minutes. Initially, shoulders are at low 2θ angles. However, this shifts to high 2θ angles after 6 minutes. Shoulders gradually disappear at 7.5 minutes and peaks become symmetric at 8 minutes.

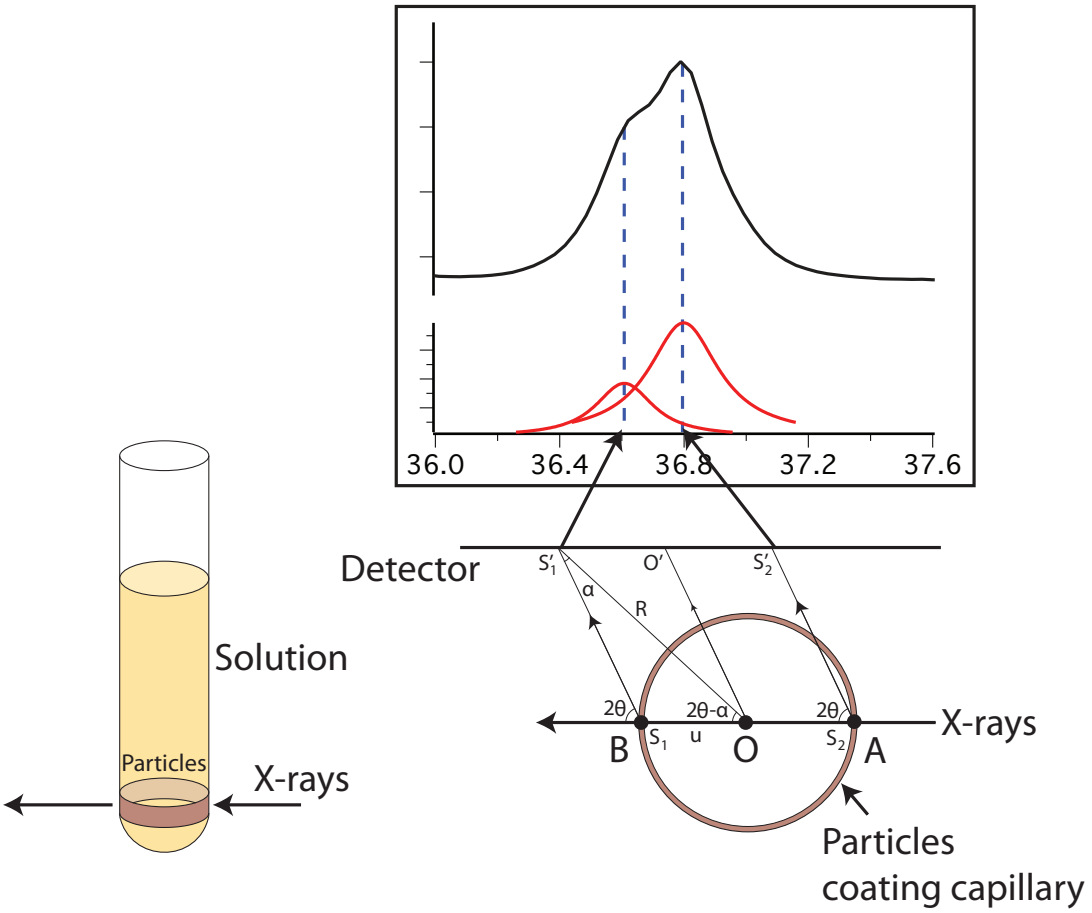

Figure 5. Shift in 2θ due to a sample displacement (±*u*) parallel to the incident beam in Debye-Scherrer geometry. A) The sample is coating the capillary walls instead of filling the entire capillary volume. B) The sample is displaced from the origin, *O*, to S_1 and S_2. The observed diffraction angle is shifted from *O'* to S'_1 and S'_2 by ±α.

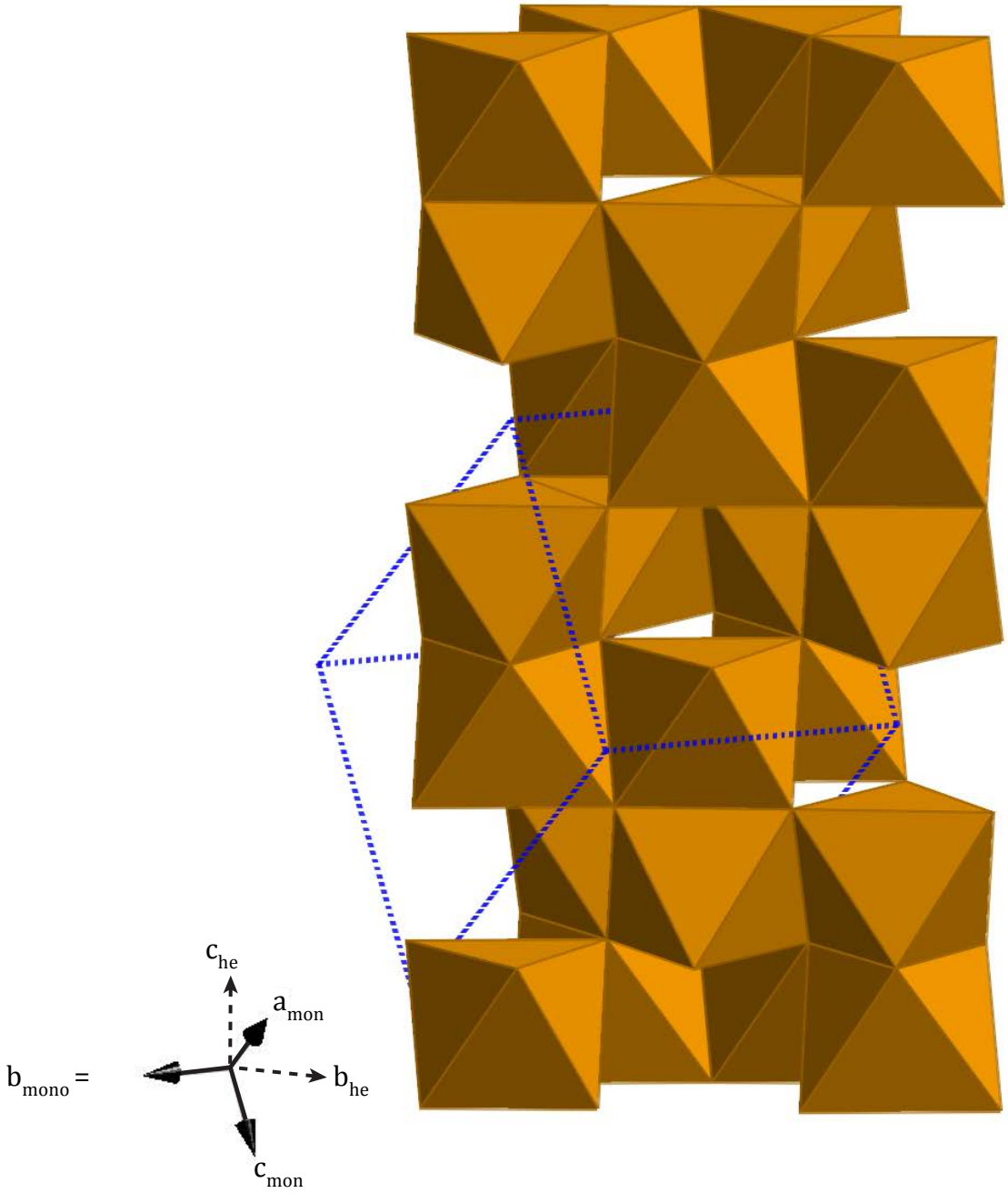

Figure 6. Crystal structure of hematite in the monoclinic setting (*I*2/*a*).

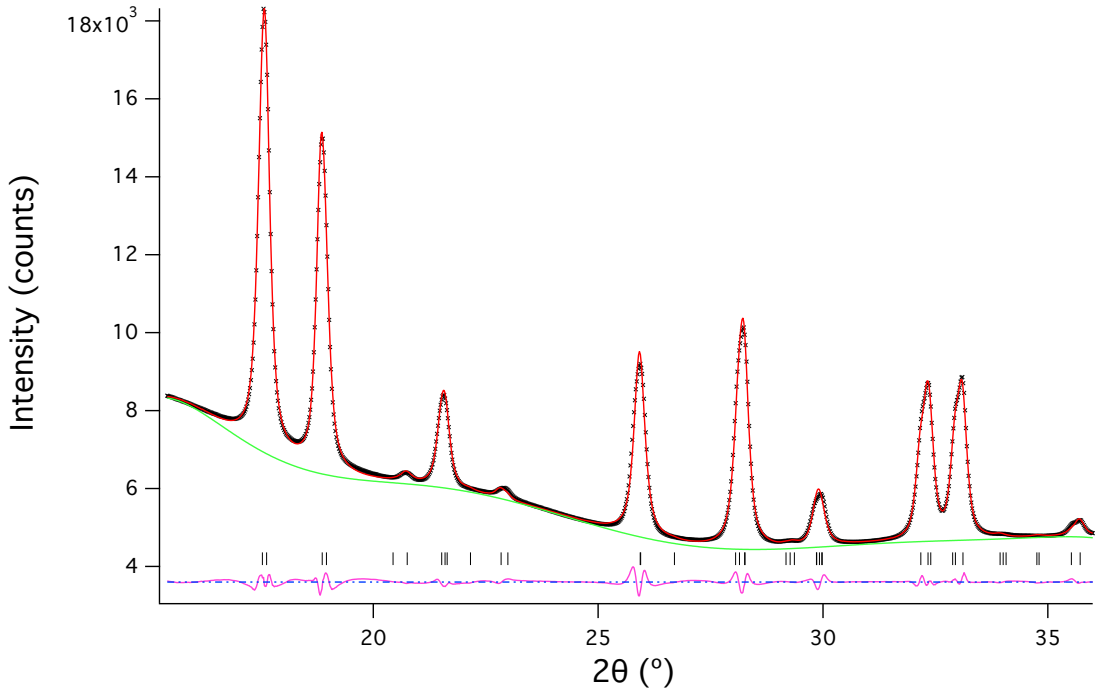

Figure 7. Observed (crosses), calculated (red line) and differences (pink line) diffraction patterns for Rietveld refinement of experiment 1 at 38 °C using space group *I*2/*a*.

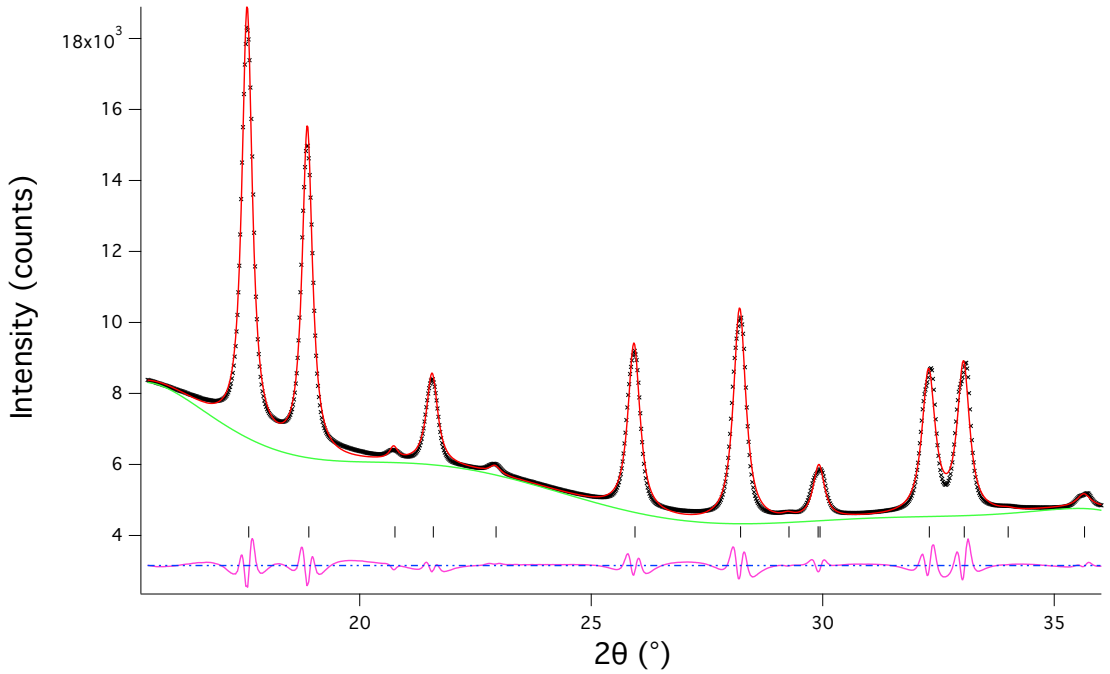

Figure 8. Observed (crosses), calculated (red line), and difference (pink line) diffraction patterns for a Rietveld refinement of experiment 1 at 38 °C using space group *R*-3*c*.

A.

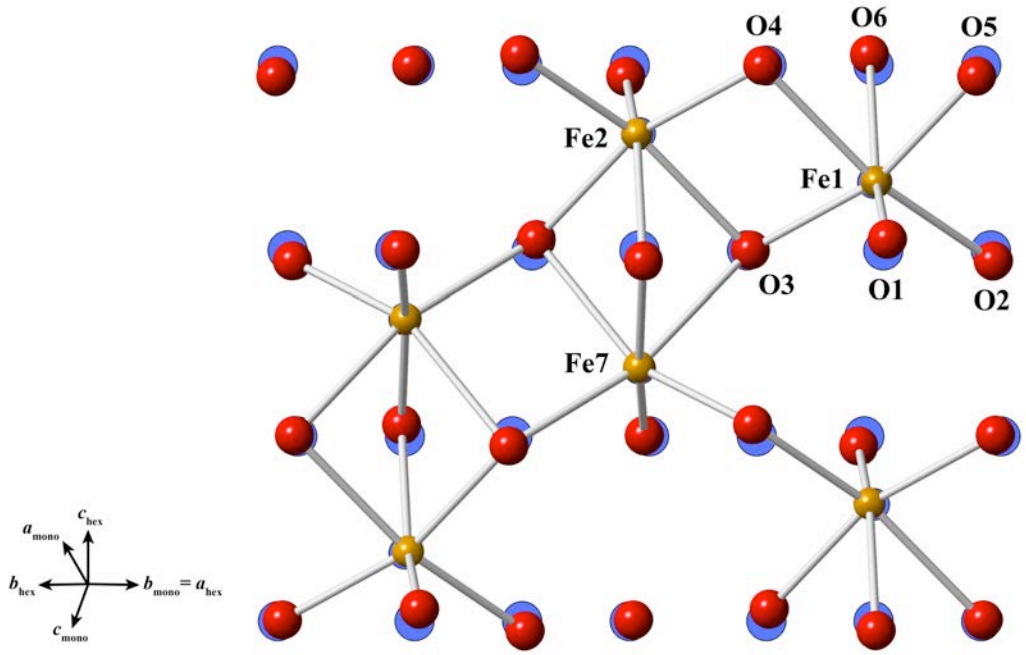

B.

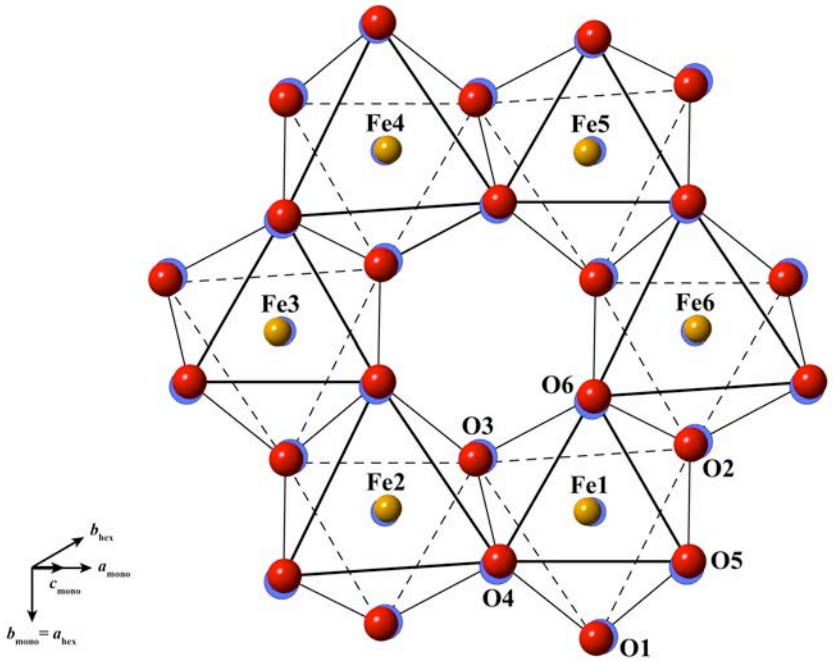

Figure 9. Crystal structure of monoclinic hydrohematite with atomic positions (Table 3). A) Projection in which the hexagonal hematite *c*-axis would be vertical shows the displacement of Fe cations (yellow) and oxygen anions (red) relative to their positions in hexagonal hematite (blue); B) Projection along the hexagonal hematite *c*-axis reveals the polyhedral distortions that violate 3-fold symmetry.

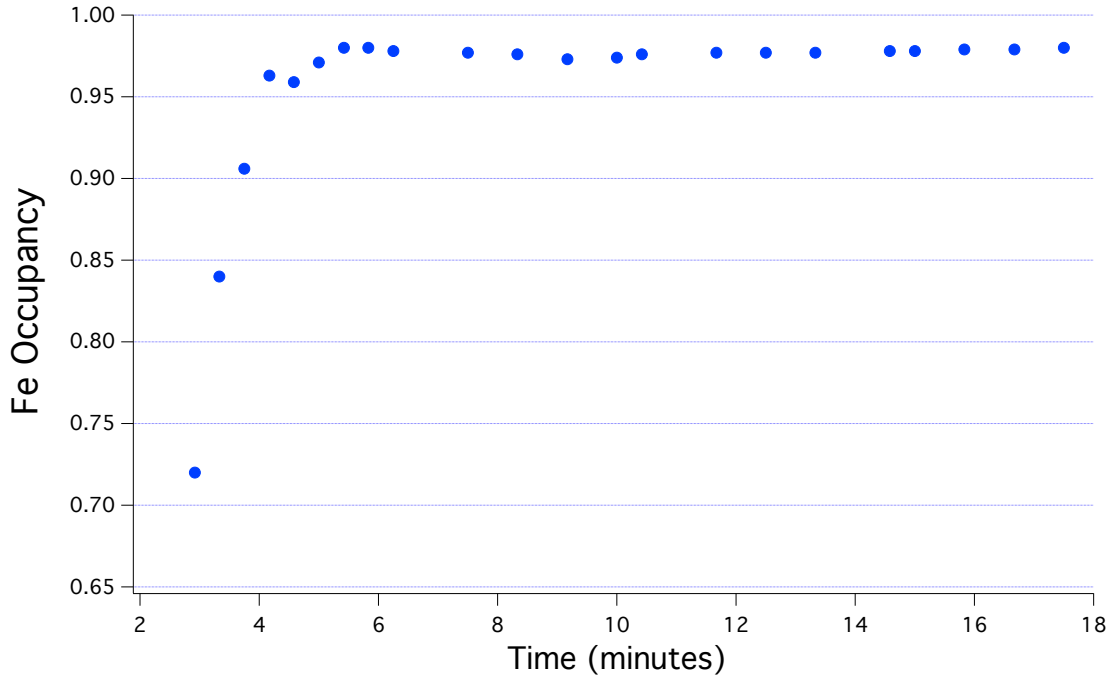

Figure 10. Refined Fe occupancy versus time at 200 °C. The Fe occupancy rapidly increases from 0.73 and but stabilizes at 0.98 after approximately 2.5 minutes.

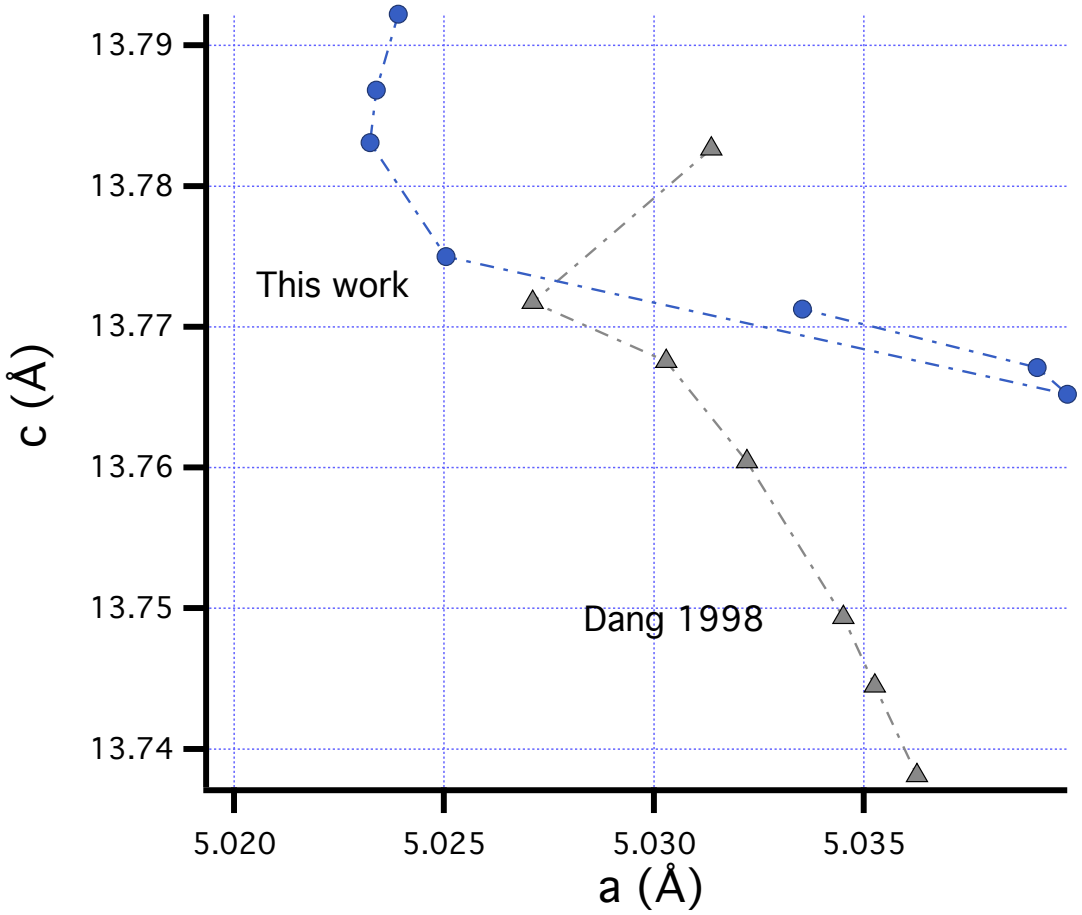

Figure 11. Time resolved X-ray data at 200 °C (blue circles). Data are shown using pseudo-hexagonal *c* and *a* unit-cell parameters for comparison to experimental data from Dang et al. 1998 (grey triangles). During our experiment, *a* and *c* initially contracted. The *a* parameter began to expand after 6 minutes. Finally, there was a second contraction in *a* at 7.5 minutes.